

1 **Mixed layer depth variability in the Red Sea**

2 Cheriyei P. Abdulla^{1*}, Mohammed A. Alsaafani^{1,2}, Turki M. Alraddadi¹, and Alaa M. Albarakati¹

3 ¹Department of Marine Physics, Faculty of Marine Sciences, King Abdulaziz University, Jeddah, Saudi Arabia.

4 ²Department of Earth & Environmental Sciences, Faculty of Science, Sana'a University, Yemen.

5

6 *Correspondence to:* Cheriyei P. Abdulla (acp@stu.kau.edu.sa)

7 **Abstract**

8 For the first time, a monthly climatology of mixed layer depth (MLD) in the Red Sea has been derived
9 based on temperature profiles. The general pattern of MLD variability is clearly visible in the Red Sea,
10 with deep MLDs during winter and shallow MLDs during summer. Transitional MLDs have been found
11 during the spring and fall. Northern end of the Red Sea experienced deeper mixing and higher MLD,
12 associated with the winter cooling of the high-saline surface waters. Further, the region north of 19° N
13 experienced deep mixed layers, irrespective of the season. Wind stress plays a major role in the MLD
14 variability of the southern Red Sea, while net heat flux and evaporation are the dominating factors in the
15 central and northern Red Sea regions. Ocean eddies and Tokar gap winds significantly alters the MLD
16 structure in the Red Sea. The dynamics associated with the Tokar gap winds leads to a difference of more
17 than 20 m in the average MLD between the north and south of the Tokar axis.

18 **Keywords:** Mixed layer depth, Red Sea, Eddies, Tokar gap winds, Air-Sea interaction.

19 **1 Introduction**

20 The surface mixed layer is a striking and universal feature of the open ocean where the turbulence
21 associated with various physical processes leads to the formation of a quasi-homogeneous layer with
22 nearly uniform properties. The thickness of this layer, often named mixed layer depth (MLD), is one of
23 the most important oceanographic parameters, as this layer directly communicates and exchanges energy
24 with the atmosphere and therefore has a strong impact on the distribution of heat (Chen et al., 1994),
25 ocean biology (Polovina et al., 1995) and near-surface acoustic propagation (Sutton et al., 2014). Heat
26 and fresh-water exchanges at the air-sea interface and wind stress are the primary forces behind turbulent
27 mixing. The loss of heat and/or freshwater from the ocean surface can weaken the stratification and
28 enhance the mixing. Similarly, a gain in heat and/or freshwater can strengthen the stratification and reduce
29 the mixing. The shear and stirring generated by the wind stress enhance the vertical mixing and play a
30 major role in controlling the deepening of the oceanic mixed layer. Further, the stirring associated with
31 turbulent eddies predominantly changes the mixing process, mainly along the isopycnal surfaces where
32 stirring may occur with minimum energy (de Boyer Montegut et al., 2004; Hausmann et al., 2017; Kara
33 et al., 2003).

34 The Red Sea is a semi-enclosed narrow basin connected to the Indian Ocean through the Gulf of Aden. It
35 is one of the important deep water formation regions, and its signature reaches into the Indian Ocean
36 (Beal et al., 2000). The Red Sea is surrounded by extremely hot arid lands and has a relatively strong
37 evaporation rate (2 m yr^{-1}) with nearly zero precipitation (Albarakati and Ahmad, 2013; Bower and Farrar,
38 2015; Sofianos et al., 2002). This region experiences strong seasonality in its atmospheric forcing and
39 buoyancy. These characteristics, along with the lack of river input, make the Red Sea one of the hottest
40 and most saline ocean basin in the world. The narrow and semi-enclosed nature of the basin, the presence
41 of multiple eddies, strong evaporation, lack of river input and very weak precipitation, seasonally
42 reversing winds, etc. lead to complex dynamical processes in the Red Sea (Aboobacker et al., 2016; Yao
43 et al., 2014a, 2014b; Zhai and Bower, 2013; Zhan et al., 2014).

44 The increase in number temperature and salinity profiles in recent years enhanced the study of MLD
45 structure and its variability, both globally (de Boyer Montegut et al., 2004; Kara et al., 2003; Lorbacher

46 et al., 2006) and regionally (Abdulla et al., 2016; D’Ortenzio et al., 2005; Keerthi et al., 2012, 2016; Zeng
47 and Wang, 2017). The Red Sea has been investigated for many years with an emphasis on its different
48 physical features. But, no detailed investigation on MLD variability has been documented so far in the
49 Red Sea, except few studies addressing the hydrography and vertical mixing of localized areas (Alsaafani
50 and Shenoi, 2004; Bower and Farrar, 2015; Carlson et al., 2014; Yao et al., 2014b).

51 In this work, an MLD climatology is produced for the first time based on in situ observations. Further,
52 the roles of atmospheric forces and oceanic eddies on the changes of the MLD have been investigated.
53 The following sections are arranged as: Sect. 2 describes the datasets used and methodology. The
54 subsequent sections discuss the observed MLD variability in the Red Sea (Sect. 3), the role of the major
55 forces on the MLD variability (Sect. 4), the impact of eddies on MLD changes (Sect. 5) and the influence
56 of Tokar gap winds (Sect. 6). The main conclusions of the present work are given in the final section.

57 **2 Data and methods**

58 **2.1 Datasets**

59 Temperature and salinity profiles from different sources are collected, which are measured using CTD
60 (conductivity-temperature-density profiler), PFL (autonomous profiling floats including ARGO floats),
61 XBT (expendable-bathy-thermograph) and MBT (mechanical-bathy-thermograph). The World Ocean
62 Database (<https://www.nodc.noaa.gov/OC5/SELECT/dbsearch/dbsearch.html>) is the main source with
63 larger number of profiles. Apart from this, data from Coriolis data center
64 (<http://www.coriolis.eu.org/Data-Products/Data-Delivery/Data-selection>) and several cruises conducted
65 by individual institutions are also used in this analysis. The bathythermograph profiles were depth-
66 corrected based on Cheng et al., (2014). A total 13,891 temperature profiles were made for the Red Sea
67 (approximately 14 % of these profiles have salinity measurements) from 1934 to 2017.

68 These profiles are quality checked according to the procedure given in Boyer and Levitus (1994). In the
69 duplicate check, all the profiles within a 1 km radius and taken on the same day are considered duplicates

70 and are removed from the main dataset. The levels in the profile with large inversions in temperature
71 (inversion $\geq 0.3^\circ\text{C}$) are flagged and removed. If three or more inversions are present, then the entire
72 profile is removed. The levels with extreme gradients $\geq 0.7^\circ\text{C}$ are also removed from the profile. Since
73 the present work is more focused on the changes in the upper layer of the ocean (from the surface to a
74 150 m depth), profiles with low resolutions in the upper layers are removed. Almost 50 % of the profiles
75 have resolutions of < 5 m, while 7 % of the profiles have poor resolutions (resolutions of > 25 m).

Deleted: The number of profiles removed at each step of the quality check is tabulated in Table S1.

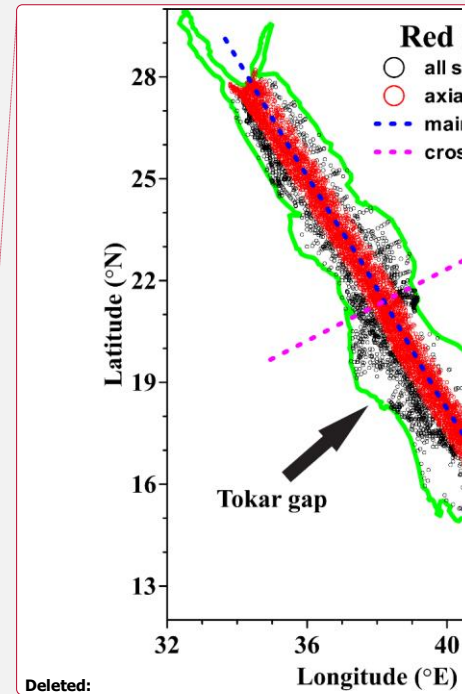
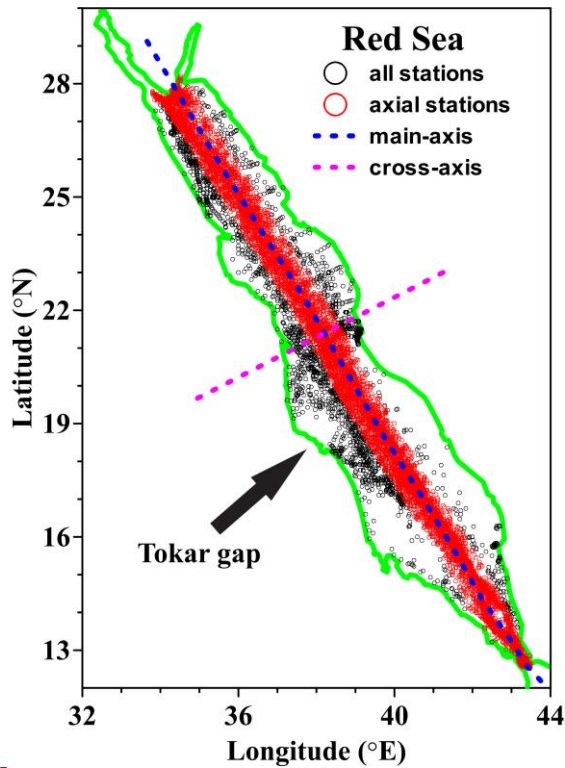
76 [Out of the total of 13,891 profiles analysed, 11,212 profiles passed the quality check from CTD \(690\),](#)
77 [PFL \(1385\), XBT \(5507\) and MBT \(3630\), and the spread is shown in Fig. 1.](#) More than 80 % of these
78 profiles are positioned along the middle of the Red Sea, with a sufficient number of profiles for each
79 month ([Fig. S1](#)). The yearly and monthly distributions of the temperature profiles lie along the middle of
80 the Red Sea and are given in the supplementary material ([Fig. S2-S3](#)). As part of the quality check, 2679
81 profiles were removed from the main dataset. A total of 2063 salinity profiles are available for the entire
82 Red Sea ([Fig. S4](#)). MLD is estimated based on the temperature profiles due to the increased number and
83 sufficient monthly coverage comparing to that of salinity. The [distribution](#) of the temperature profiles
84 used in this analysis is shown in [Fig. 1](#).

Deleted: A total of 11,212 profiles passed the quality check from CTD (690), PFL (1385), XBT (5507) and MBT (3630), and the spread is shown in Fig. 1.

Deleted: Tables 2-3

Deleted: Table 4

Deleted: spread



Deleted:

93

94 **Figure 1.** The locations of temperature profiles in the Red Sea. Black circles denote all available profiles,
 95 while red circles denote the profiles close to the main-axis that used for climatology calculation. The blue
 96 (magenta) dashed line indicate main-axis (cross-axis) of the Red Sea.

97 The monthly mean values of heat fluxes and wind stress data are provided by Tropflux at a $1^\circ \times 1^\circ$ spatial
 98 resolution for the period 1979-2016, which are used to check the influence on MLD variability
 99 (http://www.incois.gov.in/tropflux_datasets/data/monthly/). Tropflux captures better variability and less
 100 bias than the other available fluxes and wind stress products (Praveen Kumar et al., 2012, 2013). Since

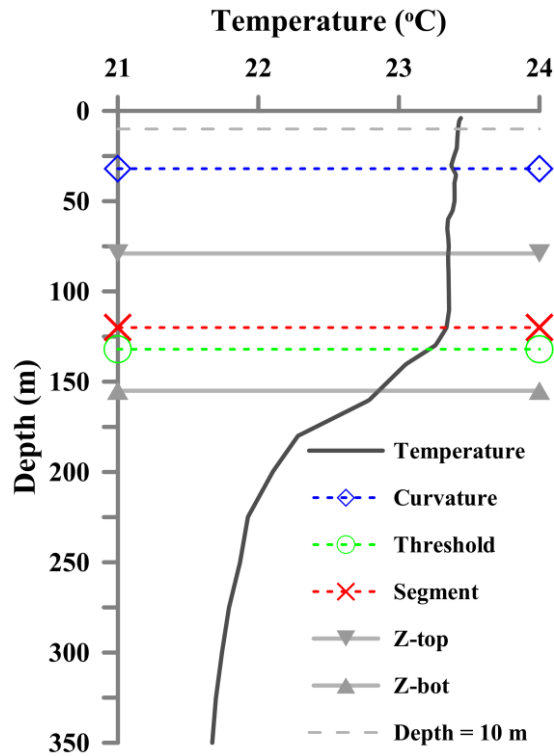
102 evaporation is not provided by Tropflux, the monthly mean values of evaporation from OAflux (from
103 1979 to 2016 and $1^\circ \times 1^\circ$ spatial resolution) are used
104 (ftp://ftp.whoj.edu/pub/science/oaflux/data_v3/monthly/evaporation/). The TRMM (Tropical rainfall
105 measuring mission, <https://pmm.nasa.gov/data-access/downloads/trmm>) satellite provided the
106 precipitation information for every $0.25^\circ \times 0.25^\circ$ grid and 3-hourly to monthly time scale from 1997 to
107 2016 (TRMM monthly 3B43_V7 product is used). Monthly climatology of heat flux, evaporation,
108 precipitation and wind stress are calculated. The period of precipitation data used for climatology
109 calculation is shorter than other parameters. The present analysis is focusing on the seasonal timescale,
110 and [therefore](#), shorter data period will not significantly affect the results.

111 The daily sea level anomaly (SLA) maps are provided by AVISO (www.aviso.oceanobs.com). These data
112 are the merged product of satellite estimates from TOPEX/Poseidon, Jason-1, ERS-1/2, and Envisat and
113 are globally available for every $0.25^\circ \times 0.25^\circ$ grid from the year 1992 to present (Ducet et al., 2000; Le
114 Traon and Dibarboure, 1999). The SLA maps are used to describe the eddy distribution in the Red Sea.
115 Climate Forecast System Reanalysis (CFSR) provided hourly wind product from 1979 to 2010 at every
116 $0.312^\circ \times 0.312^\circ$ grid (<https://rda.ucar.edu/datasets/ds093.1/#!access>) which is validated in the Red Sea by
117 Aboobacker et al., (2016). CFSR hourly wind at 10 m above the surface is used to study the Tokar gap
118 winds.

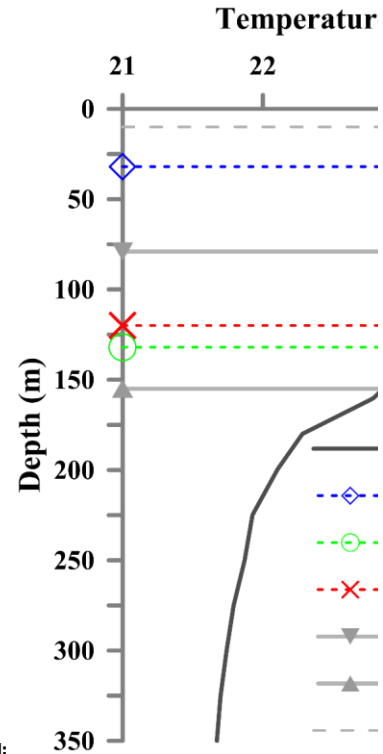
119 2.2 Methods

120 [The MLD can be estimated based on different methods. The Fig.2 shows a sample temperature profile](#)
121 [collected on 19th January 2015 from Red Sea \(24.9° N, 35.18 °E\), with short-range gradients within the](#)
122 [mixed layer. This gradient could rise from instrumental errors or turbulence in the upper layer. The](#)
123 [curvature method \(Lorbacher et al., 2006\) identified MLD at 32 m, due to the presence of a short range](#)
124 [gradient at this depth. The threshold method \(de Boyer Montegut et al., 2004\) detected MLD at 130 m](#)
125 [\(threshold = 0.2 °C\), while the segment method \(Abdulla et al., 2016\) identified MLD at 120 m. The](#)
126 [segment method based MLD could be considered as a reliable estimate comparing to both curvature](#)
127 [\(under estimation\) and threshold method \(over estimation\). The segment method first identifies the](#)

portion of the profile with significant inhomogeneity where the transition from a homogeneous layer to inhomogeneous layer occurs. Then, this portion of the profile is analyzed to determine the MLD (detailed procedure of the estimation technique is given Abdulla et al., 2016). In the present study, MLD is estimated based on the segment method, which is found to be less sensitive to short-range disturbances within the mixed layer (Abdulla et al., 2016). This method first identifies the portion of the profile (segment) where the transition from a homogeneous layer to inhomogeneous layer occurs. Then, this segment is analyzed to determine the MLD.



Deleted: Different approaches are available for MLD estimation. The MLD calculated based on three methods for a schematic temperature profile is shown in Fig. 2. Short-range gradients are manually inserted at different depths within the mixed layer, which can be expected from instrumental errors or due to turbulence in the upper layer. The threshold method (de Boyer Montégut et al., 2004) detected MLD at 26 m depth (threshold = 0.2 °C), while curvature method (Lorbacher et al., 2006) identified MLD at ~10 m. The segment method (Abdulla et al., 2016) identified MLD at 120 m, which could be considered as a reliable estimate comparing to both curvature and threshold method. The segment method first identifies the portion of the profile with significant inhomogeneity where the transition from a homogeneous layer to inhomogeneous layer occurs. Then, this portion of the profile is analysed to determine the MLD (detailed procedure of the estimation technique is given Abdulla et al., 2016). In the present study, MLD is estimated based on the recently introduced segment method, which is found to be less sensitive to short-range disturbances within the mixed layer (Abdulla et al., 2016). This method first identifies the portion of the profile (segment) where the transition from a homogeneous layer to inhomogeneous layer occurs. Then, this segment is analyzed to determine the MLD.



Deleted:

160 [Figure 2. The MLD estimated for a sample temperature profile based on curvature, threshold, and](#)
161 [segment methods. The Z-top and Z-bot respectively represents the top and bottom ends of the portion of](#)
162 [the profile with significant inhomogeneity.](#)

163 The availability of profiles is denser along the middle of Red Sea during all months. The present analysis
164 is performed for the profiles that fall within 0.5 degrees to the east and west of the main axis that, running
165 along almost the middle of the Red Sea (hereafter called the “main axis”), has the advantage of a sufficient
166 number of profiles for every month. The main axis of the Red Sea is inclined to the west, with respect to
167 true north, by ~30 degrees. For this reason, instead of zonally averaging, the climatology is calculated by
168 averaging the MLDs in an inclined direction parallel to the “cross-axis” (Fig. 1). The MLD is estimated
169 for the individual profiles, and then, the monthly climatology is calculated every 0.5° from south to north
170 (13_°N to 27.5_°N).

171 The heat flux, evaporation, precipitation and wind stress are interpolated to 0.5°x0.5° spatial grid to match
172 with MLD climatology with the help of climate data operator (CDO) tool available at
173 <http://www.mpimet.mpg.de/cdo>. The changes in surface water buoyancy forces is calculated following
174 (Turner, 1973)

$$B_0 = (C_p^{-1} g \alpha \rho_0^{-1} Q_{net}) + (-1 * g \beta s (E - P)) = B_{0T} + B_{0H} \quad (1)$$

176 where C_p = water heat capacity, g = acceleration due to gravity, α =thermal expansion coefficient, ρ_0 =
177 density of surface water, Q_{net} = net heat flux at the sea surface, β = haline contraction coefficient, s =salinity
178 of surface water, E = evaporation rate, and P =precipitation. In Eq. (1), B_{0T} and B_{0H} , respectively, represent
179 the thermal and haline components of the buoyancy force. For ease of explanation, the Red Sea is divided
180 into southern (13° N-18° N), central (18° N-23° N) and northern (23° N-28° N) regions and the seasons
181 defined as winter (Dec-Feb), spring (Mar-Apr), summer (May-Aug) and fall (Sep-Nov).

Deleted:

Deleted:

184 **3 Results and discussion**

185 **3.1 MLD variability in the Red Sea**

186 The Red Sea exhibits strong seasonal changes in its MLD, with deeper mixed layers during the winter
187 and shallower ones during the summer, with gradual changes from deeper to shallower and vice versa in
188 the transitional months. [A Hovmoller diagram of the monthly MLD climatology is presented in Fig. 3.](#)
189 [The deepest MLD is observed in February and the shallowest during May-Jun. A significant annual](#)
190 [variability is observed in the Red Sea. The maximum value of climatological mean MLD is observed in](#)
191 [February at the northern Red Sea while the minimum noticed at various instances, especially during](#)
192 [summer months. The MLD of individual profiles in the northern Red Sea has a wide range values from](#)
193 [40 to 120 m mainly due to the presence of active convection process, while some of the profiles show](#)
194 [MLD deeper than 150 m in consistence with Yao et al., \(2014\). Apart from the northern deep convection](#)
195 [region, the south-central Red Sea between 18 °N-21 °N \(53+/-5 m\) and 14 °N-16 °N \(48+/-9 m\) also](#)
196 [experienced deeper MLDs during the winter, which is separated by a shallower MLD around 17 °N \(44+/-](#)
197 [14 m\). During July to September, the region around 19° N experienced a deeper mixed layer in contrast](#)
198 [with the general pattern of summer shoaling over the entire Red Sea.](#)

199

Deleted: A Hovmoller diagram of the monthly MLD climatology is presented in Fig. 2. The deepest MLD is observed in February; the shallowest, during May-Jun. A significant annual variability is observed in the Red Sea. The maximum value of climatological mean MLD is observed in February at the northern Red Sea while the minimum noticed at various instances, especially during summer months. The MLD of individual profiles in the northern Red Sea has a wide range values from 40 to 120 m mainly due to the presence of active convection processes, while some of the profiles show MLD deeper than 150 m. Numerical simulations by Yao 2014 winter, Osipov 2017 also reported similar results. Apart from the northern deep convection region, the south-central Red Sea (14° N-21° N) also experienced deeper MLDs during the winter, with mean MLD 60+/- 13 m. In contrast to the general pattern of shoaling during the summer, the region around 19° N experienced a deeper mixed layer from July to September.

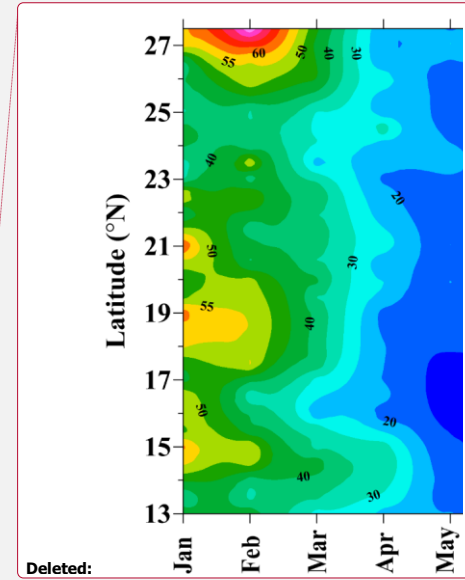
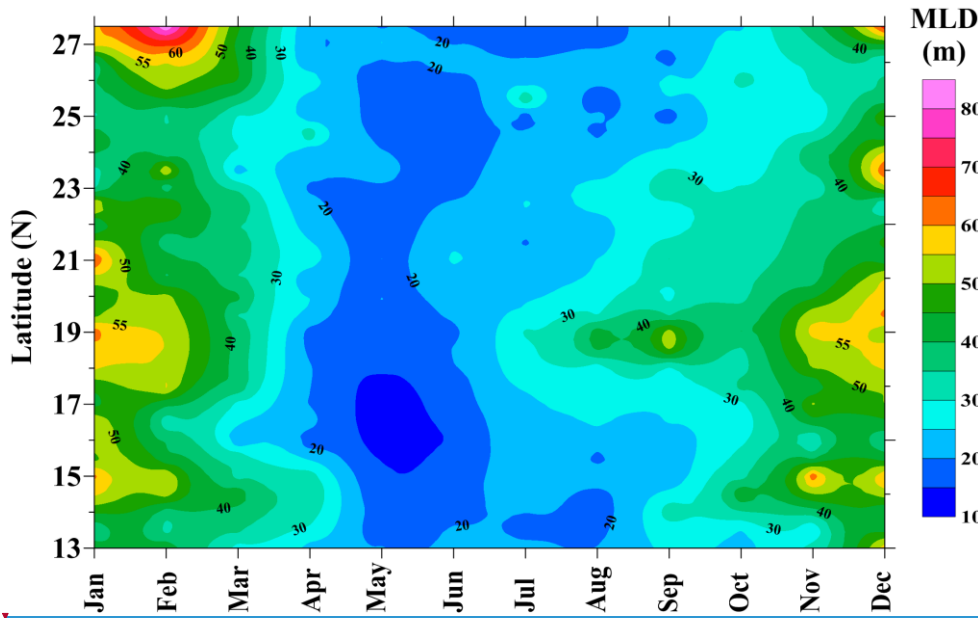


Figure 3. Hovmoller diagram of the MLD climatology along the axis of Red Sea.

The deepening of the MLD begins in October throughout the Red Sea. The winter cooling and its associated convection strengthen by December, with an average MLD > 50 m. Compared to other parts of the Red Sea, during November and December, relatively shallower MLDs were witnessed at approximately 16° N-17° N, and 24.5° N-26.5° N. The winter deepening of the MLDs intensifies by January and continues throughout February. In contrast to the general pattern of deeper MLDs in the northern latitudes, the area between 24.5° N and 26.5° N shows a relatively shallow MLD almost throughout the year, especially in the winter.

The mixed layer starts to shoal gradually by the end of February, and the MLDs of most areas decrease to 20±7 m by April. Summer shoaling is comparatively stronger in the 15° N-18° N latitude band, and

228 the detected mean MLD is < 15 m. Individual observations revealed that many profiles have MLDs < 5
229 m. In general, the shallow mixed layers are predominant from April to September, while this prevails
230 until October in the far north. In the south-central Red Sea, the shallow mixed layer exists for only a short
231 period, from April to June.

232 3.2 Major forces controlling the MLD variability

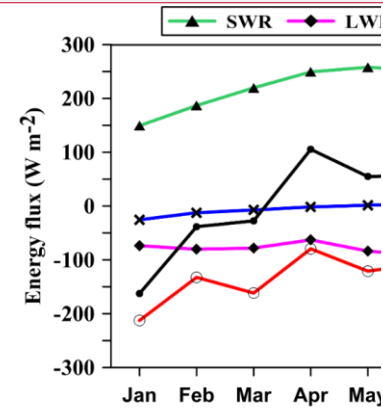
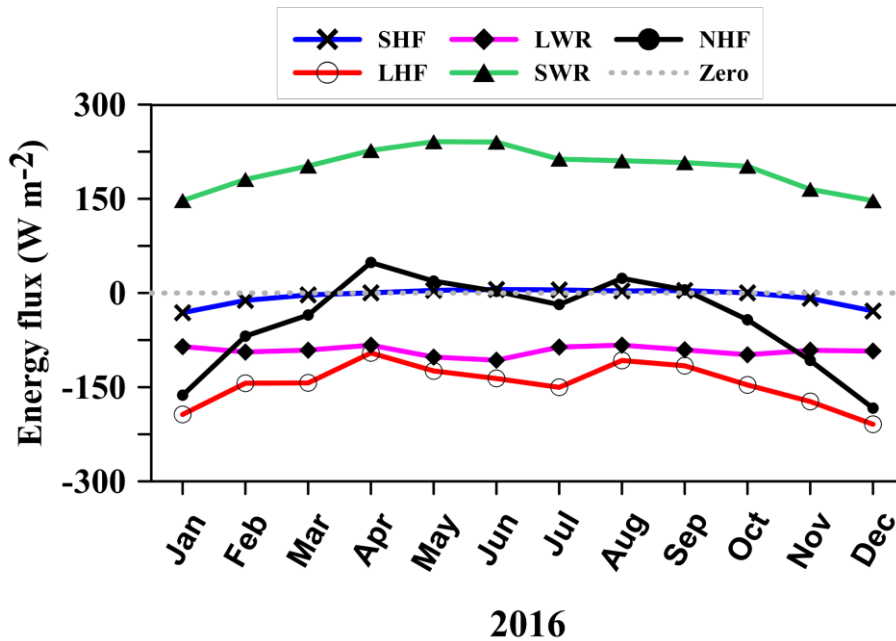
233 MLD is directly influenced by changes in the net heat flux (NHF), fresh-water flux (E-P) and wind stress.
234 The different terms that contribute to NHF are given in Fig. 4 for a sample year 2016 in the central Red
235 Sea. On an annual average basis, the incoming shortwave radiation (SWR, 202 W m⁻², positive
236 downward) is mainly balanced by LHF (latent heat flux, -126 W m⁻²) and LWR (long wave radiation, -
237 83 W m⁻²), while the SHF (sensible heat flux) is only -4 W m⁻². The net heat loss in the central Red Sea
238 is 11 W m⁻². Both the LHF and LWR are gradually increasing towards the northern Red Sea. The monthly
239 climatology of the NHF in the northern, central and southern Red Sea are given in Fig. 5a. Heat loss rises
240 above 200 W m⁻² during December-January in the northern Red Sea, with a maximum of ~250 W m⁻² at
241 the northern end of the sea in December. The annual mean of NHF is negative (heat loss) across the Red
242 Sea, except for isolated locations in the southern Red Sea with trivial heat gain (figure not shown). The
243 thermal components of the buoyancy forces calculated based on Eq. (1) show that the heat flux support
244 mixing through buoyancy loss in the northern and central Red Sea during the winter, while it opposes
245 vertical mixing due to buoyancy gain during summer. In the southern Red Sea, the effect of heat flux is
246 relatively weak.

Deleted: e

Deleted: enhance

Deleted: slightly

Deleted: diminishes



Deleted:

Figure 4. Time series of heat flux components (incoming shortwave radiation (SWR), long wave radiation (LWR), latent heat flux (LHF), sensible heat flux (SHF) and net heat flux (NHF)) for the year 2016 in the central Red Sea.

The evaporation rate in the Red Sea gradually increases from south to north (Fig. 5b). The central and northern Red Sea have higher evaporations during the winter ($\sim 6 \text{ mm day}^{-1}$) and moderate evaporations ($\sim 3 \text{ mm day}^{-1}$) during the summer. Evaporation shows weak seasonality in the southern Red Sea. Precipitation in the southern region is higher than those of the other areas of Red Sea, with maximum rainfall during July-September (Fig. 5b). The changes in buoyancy forces corresponding to fresh-water flux (haline component) are estimated based on Eq. (1), which shows that the changes support vertical mixing throughout the year and over the entire Red Sea. The thermal component is relatively higher than

263 the haline component, and the net buoyancy [flux](#) follows a more or less similar pattern of thermal
264 buoyancy [flux](#) all along the Red Sea (figure not shown). The observed variability of the above-discussed
265 parameters is consistent with findings from earlier studies (Albarakati and Ahmad, 2013; Sofianos et al.,
266 2002; Tragou et al., 1999).

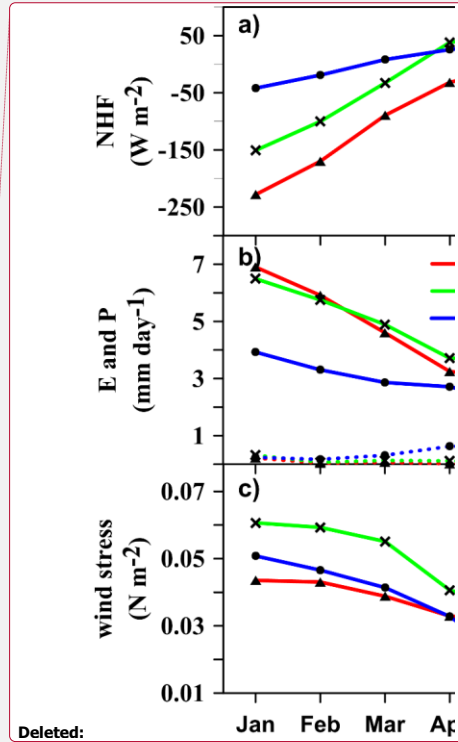
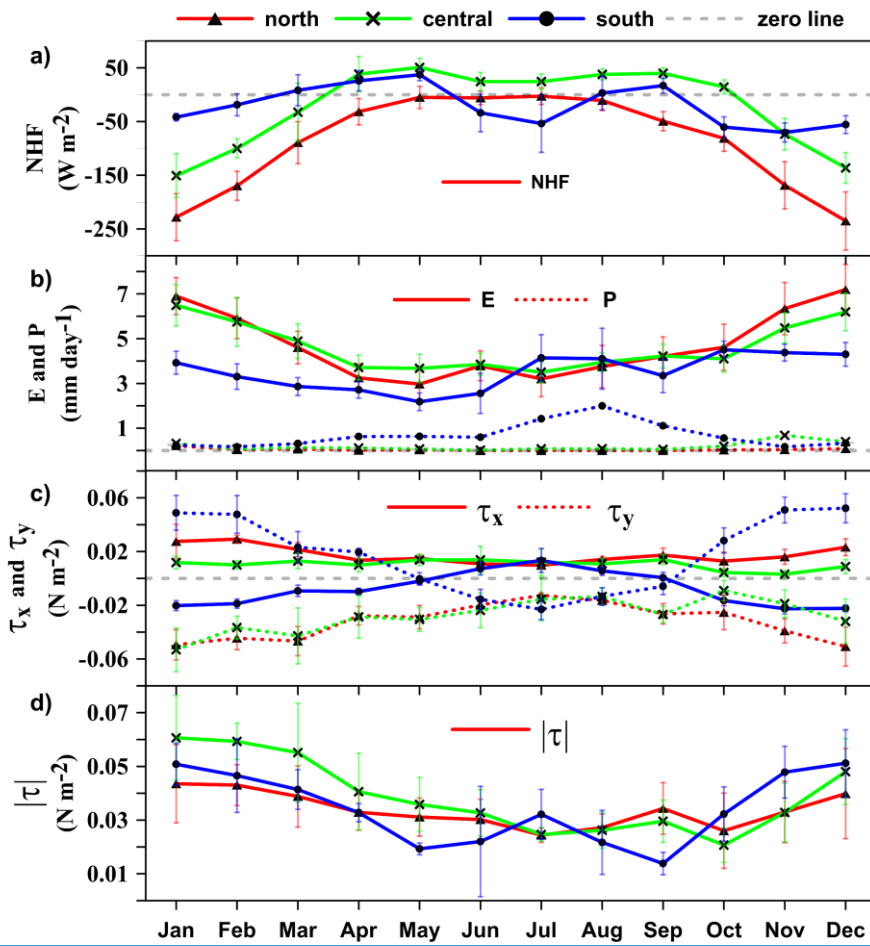


Figure 5. Monthly climatology of a) NHF, b) evaporation and precipitation, c) eastward (τ_x) and northward (τ_y) component of wind-stress, and d) magnitude of the wind stress ($|\tau|$). South, central and north regions are represented by the changes at 14° N, 21° N and 27° N.

Deleted: , and c) wind stress.

The pattern of wind stress in the Red Sea is significantly different from the other parameters. The wind stress is strong during the winter, leading to enhanced turbulence and mixing, while it is weak during the summer, resulting in a shallower mixed layer (Fig. 5c,d). Apart from that, strong surface winds blow to the Red Sea through the Tokar gap at approximately 19°N in July and August.

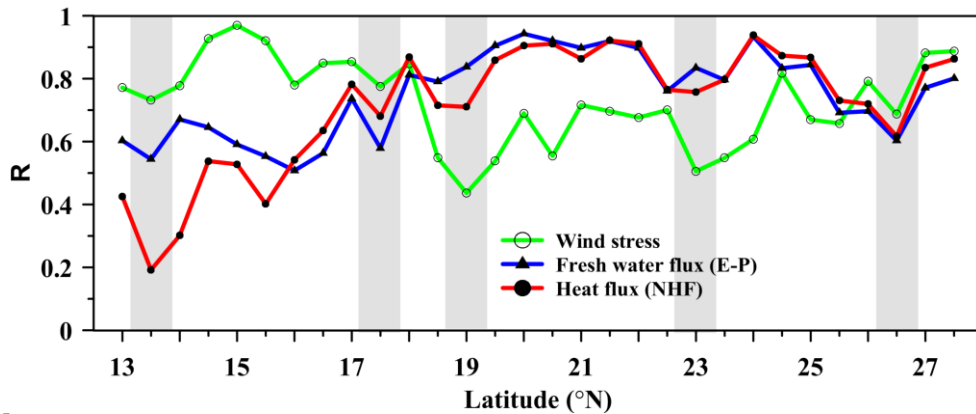
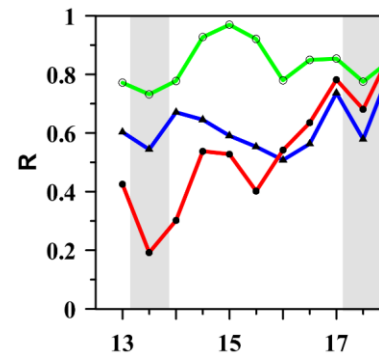


Figure 6. Correlation between major forces and MLD. Shaded regions represent locations of coinciding drops in correlation.

The correlations between MLDs and forcing factors are given in Fig. 6. The wind stress and E-P are positively correlated with MLD while the NHF is negatively correlated since as NHF (into the ocean) increases, MLD decreases. For simplicity of the figure (Fig. 6), the correlation values of all parameters are presented as positive. NHF and E-P are well correlated (>0.8) with MLD in the central and northern Red Sea, and weakly correlated in the south. Wind stress has a higher correlation (>0.8) to the south, while it is relatively weakly correlated in the central and northern Red Sea. Toward the northern end, the wind stress gradually achieves a higher correlation.

Deleted:



Deleted:

Deleted: Variability in MLD has an opposite phase to that of NHF, while the rest of the forcing are linearly phase related.

291 The results from [Fig. 5](#) and [6](#) indicate that the MLD variability of the Red Sea is dominated by wind stress
292 in the southern part, NHF (heatflux) and evaporation play a major role in the central region, while all the
293 three are influencing in the northern region. Remarkably, for all the above-discussed parameters,
294 coinciding drops are observed in the correlations at approximately 13.5° N, 17.5° N, 19° N, 23° N, and
295 26.5° N. These drops are discussed in the following section.

296 3.3 Impact of [the eddies](#)

297 Satellite altimetry maps revealed the presence of ~~multiple~~ eddies in the Red Sea which are often confined
298 to specific latitude bands. Quadfasel and Baudner (1993) reported that most of the gyres in the Red Sea
299 are concentrated in four latitude bands, approximately centered on 18° N, 20° N, 23° N and 26.5° N, and
300 some of these eddies are semi-permanent in nature. Johns et al. (1999) also reported presence of cyclonic
301 eddies in the north and south of the Red Sea and anticyclonic eddies in the central Red Sea. Clifford et al.
302 (1997) and Sofianos and Johns (2007) reported the presence of a quasi-permanent cyclonic gyre in the
303 northern Red Sea during the winter. Analyzing the SLA maps from 1992 to 2012, Zhan et al., (2014)
304 reported the presence of ~~multiple~~ eddies with both polarities in the Red Sea. The number of identified
305 eddies peaked at approximately 19.5° N and 23.5° N. The upwelling proxy constructed using MODIS
306 SST in the northern Red Sea shows the presence of frequent upwelling events at approximately 26.5° N
307 almost every year (Papadopoulos et al., 2015) indicating presence of cyclonic eddy. The extent and time
308 of the upwelling vary from year to year.

309 The eddy distribution in the Red Sea for the period from 1992-2012, based on SLA data is given in [Fig.](#)
310 [7](#), ~~where the eddies are identified using the “winding-angle” method (Zhan et al., 2014)~~. The number of
311 eddies are relatively higher in the central and northern Red Sea. The change in vertical stratification due
312 to the presence of anticyclonic eddy (AE) and cyclonic eddy (CE) for different seasons are shown in [Fig.](#)
313 [8](#). The black (green) colored curve represent the profile before (during) the eddy event. The date of
314 profiling is given in the figure caption and the stations are marked. Figure 7a & 7f shows that the presence
315 of AE during spring transformed the completely stratified upper layer to be well mixed till 50 m depth.
316 Similar instance is shown in [Fig. 8b](#) & [8g](#) where MLD changed from nearly zero to 30 m during summer.

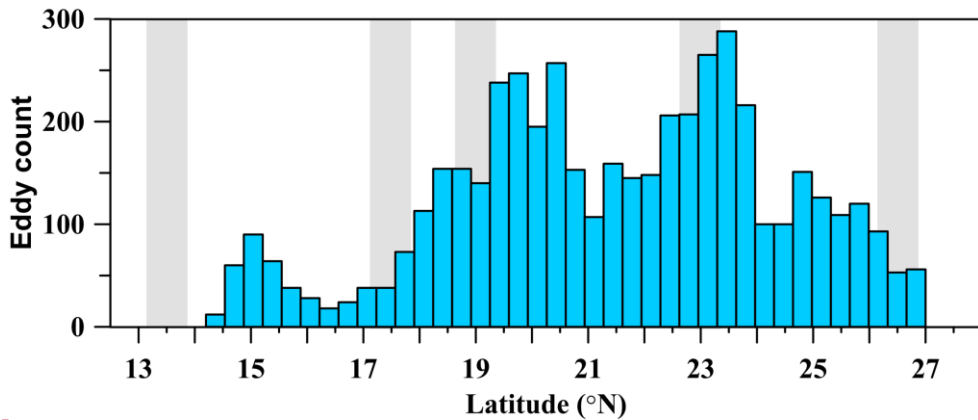
Deleted: a

Deleted: a

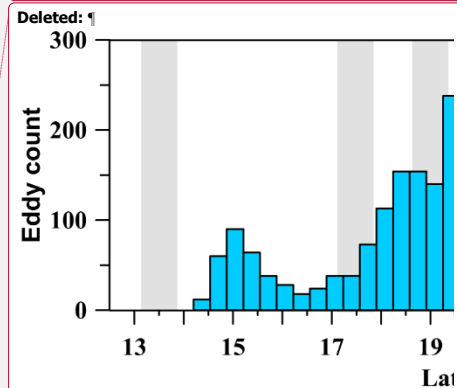
Deleted: .

320 Figure 7c & 7h show the profiles corresponding to a CE event during fall, where shoaling of MLD by
 321 ~10 m is observed. Similarly, the CE event during winter lead to shoaling of mixed layer by ~60 m (Fig.
 322 8d & 8i). Figure 8e & 8j show three profiles from single cruise collected within 12 hours which is
 323 coincided with the presence of CE and AE in a short distance, in which station A is located outside the
 324 AE, B is located inside AE and C is partly in CE. There is a difference of ~100 m in the MLD due to the
 325 presence of eddies, in a short distance. Similarly, the MLD at station C is shallower than that of A due to
 326 the presence of a CE.

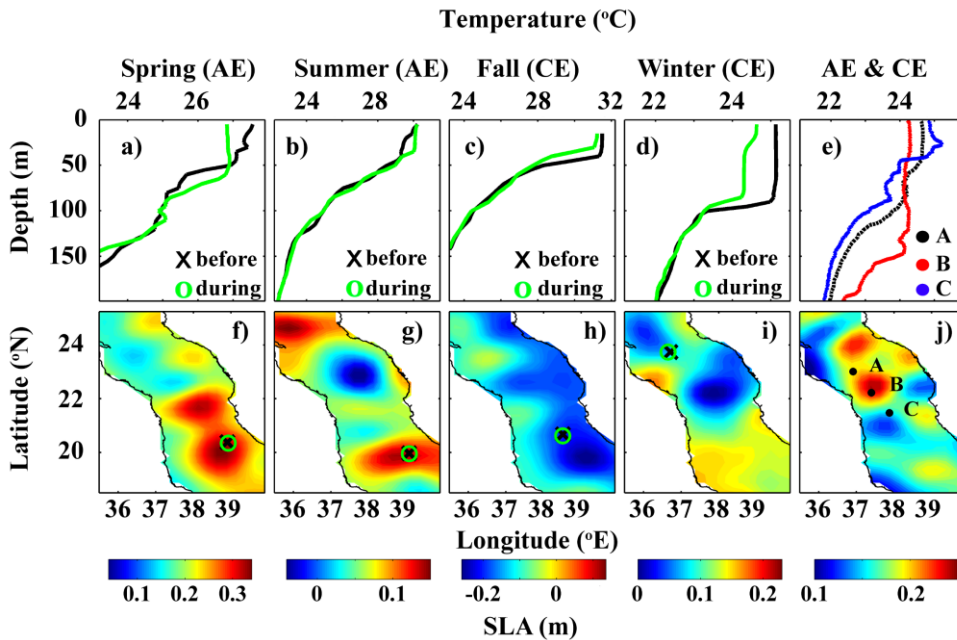
327 [Previous studies have proved that the upper ocean is efficiently re-stratified by the ocean eddies which](#)
 328 [may significantly change the MLD. The resultant effect of eddy is largely dependent on the eddy](#)
 329 [amplitude. The mixing intensity is largest at the centre of eddy and decay on average with increasing](#)
 330 [radial distance](#) (Dewar, 1986; Fox-Kemper et al., 2008; Hausmann et al., 2017; Smith and Marshall,
 331 2009). [The observed results show that the mixing associated with eddies is dominating over the existing](#)
 332 [effect of wind stress and heat flux. CE diminishes mixing through upwelling of the subsurface water while](#)
 333 [AE enhances mixing through downwelling of the surface water](#) (de Boyer Montégut et al., 2004; Chelton
 334 et al., 2004, 2011; Dewar, 1986; Hausmann et al., 2017).



Deleted: Previous researches have been proved that the upper ocean is efficiently restratified by the ocean eddies which may significantly change the MLD. The resultant effect of eddy is largely dependent on the eddy amplitude. The mixing intensity is largest at the centre of eddy and decay on average with increasing radial distance (Dewar, 1986; Fox-Kemper et al., 2008; Hausmann et al., 2017; Smith and Marshall, 2009). The CE diminishes mixing through the upwelling of the subsurface waters, while an AE enhances mixing through the downwelling of the surface waters (de Boyer Montégut et al., 2004; Chelton et al., 2004, 2011; Dewar, 1986; Hausmann et al., 2017).

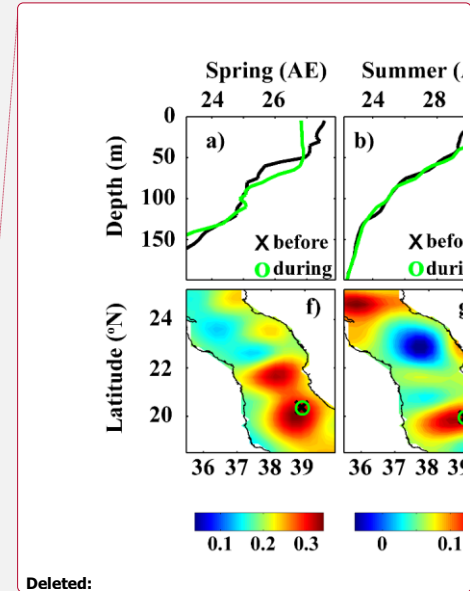


350 **Figure 7.** The number of eddies in the Red Sea derived from sea level anomaly for the period 1992-2012.
 351 The eddy count values are taken from Zhan et al., 2014. Shaded regions represent the location of
 352 correlation drops as shown in Fig. 6.



353

354 **Figure 8.** Profiles collected during (a) spring, (b) summer, (c) fall and (d) winter from the nearby stations
 355 in the Red Sea. The stations are marked on the SLA maps of the corresponding days (f-i). The “x” mark
 356 (“o” mark) represent profile collected before the appearance of the eddy (during the eddy period)
 357 and plotted in black (green) color. The dates of black and green profiles are respectively c) 11-03-2016 & 18-
 358 03-2016, e) 06-06-2016 & 13-06-2016, g) 16-09-2010 & 21-09-2010 and i) 13-12-2015 & 17-12-2015.
 359 The SLA is averaged for 5 days prior to the date of the later (green) profile. e) Temperature profiles



Deleted:

361 collected from stations A, B & C within 12 hours (6th-7th Feb 2005) and j) the average SLA map for the
362 period 4th to 7th Feb 2005.

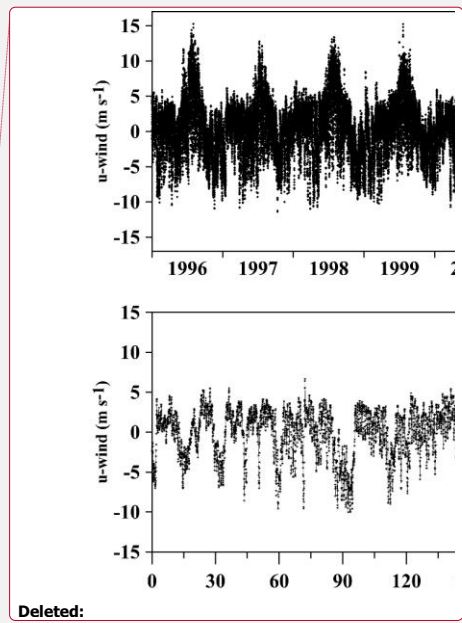
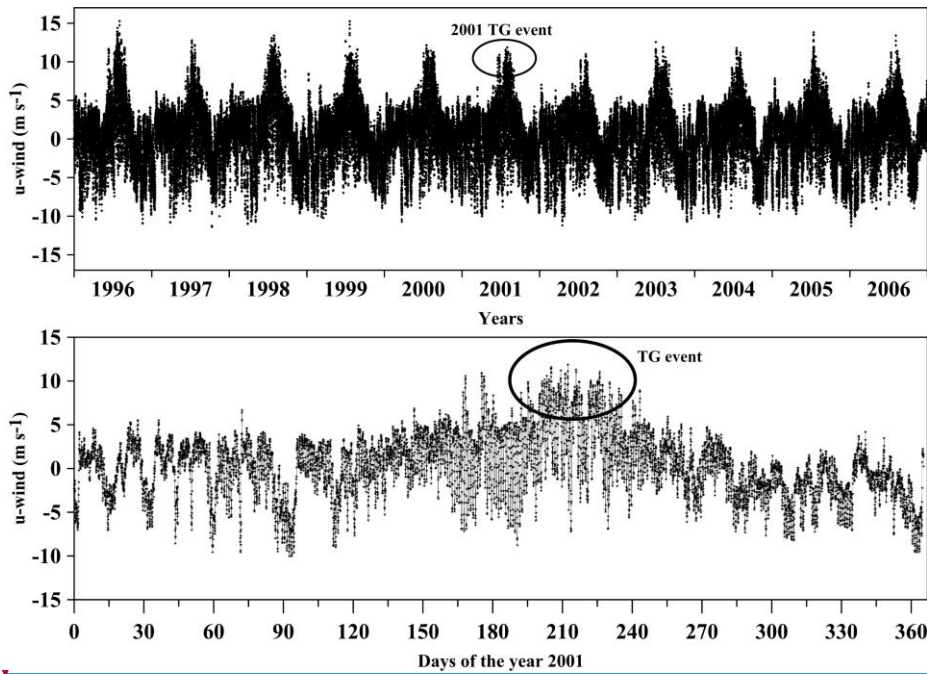
363 The coinciding drops in the correlation curves, observed at approximately 19° N, 23° N and 26.5° N are
364 well matching with the main eddy locations (Bower and Farrar, 2015; Johns et al., 1999b; Quadfasel and
365 Baudner, 1993; Zhai and Bower, 2013; Zhan et al., 2014), while those of 13.5° N and 17.5° N are not
366 (Fig. 6 and 7). The Red Sea is very narrow at 13.5° N. Moreover, complex dynamics associated with the
367 exchange of surface and subsurface waters between the Red Sea and the Gulf of Aden occur in this region.
368 The complexity of this region prevents linking the MLD variability directly to atmospheric forcing or
369 eddies. The region at approximately 17.5° N is between the two eddy-driven downwelling zones at
370 approximately 15° N and 19° N (Fig. 3). Mass conservation requires upwelling to replace the
371 downwelling water. The MLD climatology shows shallow mixed layers throughout the year at 17.5° N,
372 which could be due to possible upwelling. Further investigation is required to unveil the dynamics
373 associated with this region.

374 Rapid shoaling of the mixed layer is seen at ~26.5° N over a short distance (~100 km) adjacent to the
375 deep convection zone in the northern side. The presence of a quasi-permanent cyclonic gyre during the
376 winter (Clifford et al., 1997; Sofianos and Johns, 2007) and frequent upwelling events (Papadopoulos et
377 al., 2015) diminish the mixing in this region, leading to rapid shoaling of the mixed layer. The number of
378 eddies has a minor peak at approximately 15° N. This region has a predominance of anticyclonic eddies
379 (Zhan et al., 2014). The impact of the dominant anticyclonic eddies is visible in the MLD climatology,
380 with deeper mixed layers at approximately 15° N (Fig. 3 and 8). The above results indicate that the
381 frequent eddies in the Red Sea significantly impact the MLD variability by enhancing/diminishing the
382 mixing.

383 **3.4 Influence of Tokar gap winds during the summer**

384 The Tokar gap is one of the largest gaps in the high orography located on the African coast of the Red
385 Sea, near 19° N. Strong winds are funneled to the Red Sea through this gap which last for few days to
386 weeks. Figure 8a shows the u-component of CFSR hourly surface wind at the Tokar region from 1996 to

387 2006. From the figure, it shows that the strong wind events occur during summer every year while the
 388 intensity and duration of the event varies from year to year. Tokar gap winds frequently attain a speed of
 389 15 m s^{-1} . Previous research also show similar results (Jiang et al., 2009; Ralston et al., 2013; Zhai and
 390 Bower, 2013). Zhai and Bower (2013) reported that wind speed may reach 20 to 25 m s^{-1} based on ship
 391 based observations. Figure 8b show that the onset of 2001 Tokar event was on 20th July and continued till
 392 20th August, where the maximum wind speed occurred during this period compared to rest of the year.
 393 These strong winds generate strong turbulence in the surface water, which enhances vertical mixing.

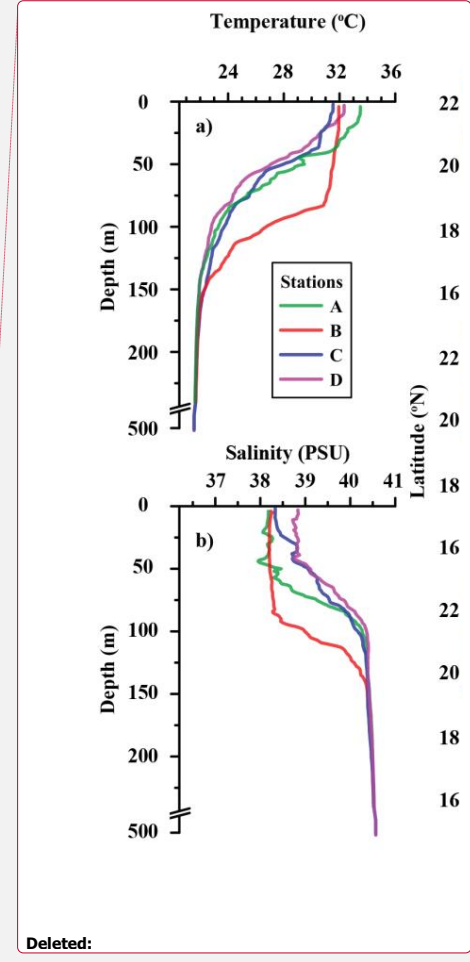
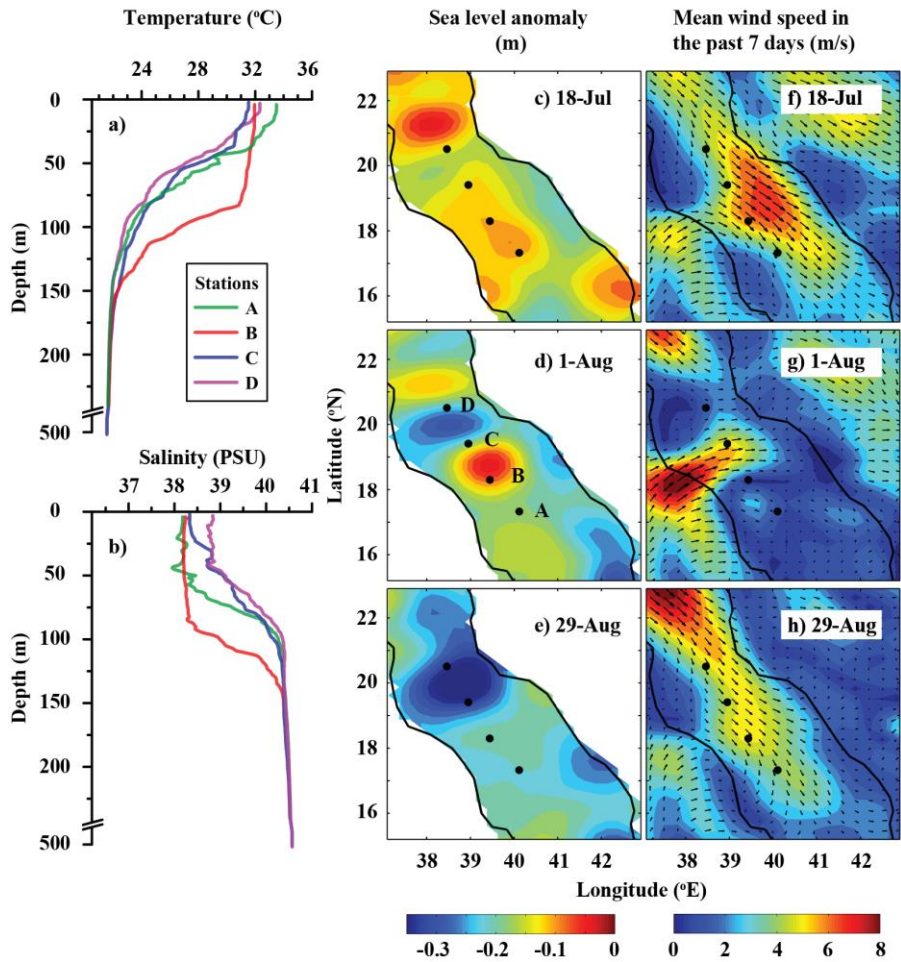


395 **Figure 9.** U-component of the [CFSR](#) hourly surface wind near the Tokar region (38.5° E , 18.5° N) a)
 396 from year 1996 to 2006 and b) for the year 2001. The ellipse indicates the TG event in the year 2001.

398 The temperature and salinity profiles measured during summer 2001 (13-14 Aug 2001), which coincided
399 with the Tokar event are shown in [Fig. 10a-b](#) (Sofianos and Johns, 2007; Zhai and Bower, 2013). The
400 signature of Tokar event is clearly visible in the satellite-derived SLA, with well-defined cyclonic and
401 anticyclonic eddies to the north and south of the Tokar gap respectively ([Fig. 10c-e](#)). Both eddies have
402 basin wide influence and radii between 70-80 kms. Corresponding wind speed pattern (averaged for the
403 previous 7 days) is shown ([Fig. 10f-h](#)). The profiles to the north and south of the jet axis display significant
404 difference in MLD, with a deeper mixed layer in the south. Station A is far from both cyclonic and
405 anticyclonic eddies and shows the expected MLD during this period. The presence of the anticyclonic
406 eddy at station B enhances strong downwelling, extending the mixing to a depth approximately 80 m. It
407 is to be noted that the entire Red Sea basin is well stratified during this period, with MLDs ranging from
408 10 m to 15 m. Stations C and D are located at the edge of the cyclonic eddy, and both have shallower
409 thermocline and mixed layer.

Deleted: (

Deleted:)



Deleted:

412
 413 **Figure 10.** (a) The CTD measured temperature and salinity profiles during 13-14 Aug 2001. (b) SLA
 414 maps and (c) wind speed and direction (averaged for the previous one week) in the Tokar region, before,

416 during and after the Tokar event. [The temperature and salinity profiles are received through personal](#)
417 [communication from](#) (Sofianos and Johns, 2007).

418 The MLDs of all the available profiles in the Tokar region before, during, just after and after a month of
419 the Tokar event are plotted in [Fig. 11](#) (profiles for the first 15 days of each month are displayed). The
420 mean MLD, standard deviation and number of profiles are given in Table 1. Before the Tokar event, the
421 southern and northern sides of the Tokar axis (18° N- 19.5° N and 19.5° N- 21° N, respectively) displayed
422 similar mixed layers ([Fig. 11a-c](#)). During the Tokar event, the southern side experienced enhanced
423 mixing, while the northern side show shallow mixed layer ([Fig. 11d-f](#)).

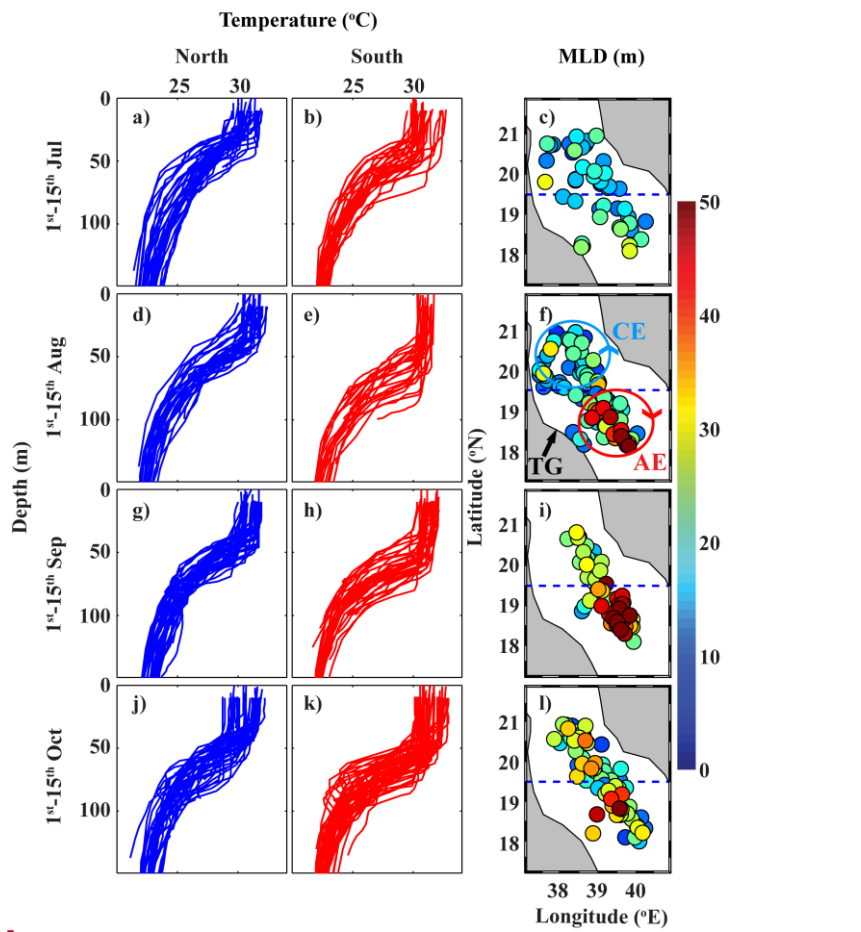
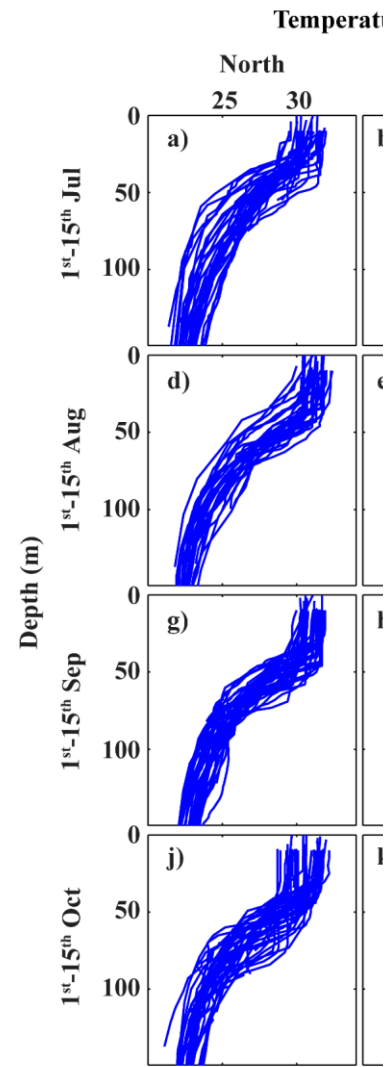


Figure 11. Temperature profiles from the north of the Tokar axis (left panel, blue curves), south of the Tokar axis (middle panel, red curves) and the corresponding MLD (right panel) during the first 15 days of each month from July to October. The dashed line passes through 19.5° N, roughly separating the north



Deleted:

430 and south of the Tokar axis. MLD of each profile is represented by the filled colors. The blue and red
 431 circles in (f) schematically represent cyclonic and anticyclonic eddies during Tokar event, respectively.

432 **Table 1.** The mean MLD in the north and south of Tokar jet axis from July to October.

1-15 th days of the Month	Mean		Standard deviation		Number of profiles	
	North	South	north	south	north	south
Jul (before)	20	26	5	8	19	12
Aug (during)	24	38	8	17	27	24
Sep (just after)	30	52	11	14	27	27
Oct (after one month)	31	34	9	12	36	30

433 The anticyclonic part of the Tokar induced eddies enhance downwelling and the associated deepening of
 434 the mixed layer along the southern side of the jet axis, while the cyclonic eddies generate upwelling and
 435 the associated shoaling of the mixed layer along the northern side. The profiles in September (just after
 436 the Tokar event) show the southern side is well mixed by the event, which leads to an average difference
 437 of 20 m in the MLDs between both sides of the Tokar axis (Fig. 11g-i). The signature of the Tokar events

438 in the MLDs (MLD difference between north and south of the jet axis) has disappeared by October (one
439 month after the Tokar event, [Fig. 11j-l](#)).

440 The mixing in the Tokar region during summer is the sum of the two mechanisms, the wind induced
441 turbulent mixing and the secondary circulation (eddies) induced by the wind. Both mechanisms act in the
442 same direction in the southern side of the jet axis resulting in enhanced mixing, while they act in opposite
443 direction in the northern side leading to reduced mixing. Further studies are required for proper
444 quantification of the contribution of each mechanism. In summary, [during the summer](#), the turbulence
445 induced by strong wind and [the impact of anticyclonic eddy](#) enhance vertical mixing [in the southern side](#)
446 [of jet axis, while the wind induced mixing is diminished by the presence of cyclonic eddy in the northern](#)
447 [side of the jet axis](#).

Deleted: s

Deleted: associated

Deleted: ies

Deleted: impact

Deleted: ¶

448 4 Conclusions

449 A detailed information on MLD variability is crucial for understanding the physical and biological
450 processes in the ocean. The goals of this study were to produce a climatology record of MLD for the Red
451 Sea and to investigate the role of major forces on MLD changes. With the help of in situ temperature
452 profiles from CTD, XBT, MBT and profiler float measurements, the MLD variability in the Red Sea has
453 been explored for the first time and the MLD climatology is produced for every 0.5 degrees along the
454 main axis. [The climatology](#) reasonably captured all the major features [of MLD variability in the Red Sea](#).
455 The present work provides a [climatological mean](#) of the MLD structure in the Red Sea and its seasonal
456 variability. Influences of wind stress, heat flux, evaporation and precipitation are explored. Further, the
457 impact of the Tokar gap jet stream winds, [the](#) eddies and the upwelling events in the northern Red Sea are
458 investigated.

Deleted: Averaging the MLDs can result in slightly lower values,
but

Deleted: t

Deleted: climatology

Deleted: general picture

Deleted: also

459 A deep ventilation process associated with the winter cooling is observed across the entire Red Sea during
460 the months of December to February ([Fig. 3](#)). Similarly, very shallow MLDs [associated with increased](#)
461 [short-wave radiation](#) are detected all along the region from May to Jun. The climatological winter MLD
462 ranges from ~40 to 85 m (in January). Similarly, the climatological summer MLD varies from 10 to ~20

Deleted: strong stratification

475 m (in June), which may reach to >40 (in July). The mixed layer becomes deeper toward the north, even
476 though the pattern is not linear with increasing latitude. The largest amplitude of variability is observed
477 at the tip of the northern Red Sea which is associated with strong deep convection during the winter and
478 shoaling during the summer. The region at approximately 19° N experienced deeper MLD than typical of
479 elsewhere in the Red Sea. This region experienced enhanced mixing during winter by surface cooling,
480 and during summer by the Tokar gap wind induced turbulent mixing and the formation of anticyclonic
481 eddy. The deepest mixed layer is observed at the northern tip of Red Sea during the winter, but the deep
482 nature of northern mixed layer is almost limited to the winter months.

Deleted: Sea, and

Deleted: than average MLD for most of the year

Deleted: This region experienced enhanced mixing during winter by surface cooling during winter, and during summer by the Tokar gap wind induced turbulent mixing and the formation of anticyclonic eddy during summer.

483 Correlation analyses between MLD and forcing factors displayed the influence of major forces on MLD,
484 from north to south of the Red Sea. In general, the wind stress mainly controls the MLD variability in the
485 southern part of the Red Sea, heat flux and evaporation dominate in the central region, and all the three
486 forces contribute in the northern region. Coinciding drops are observed in the correlations for all the
487 selected forcing factors around the previously reported main eddy locations. In these locations, eddies
488 override the controls of the other main forces, namely, wind stress, heat flux and fresh-water flux. The
489 quasi-permanent cyclonic gyre and upwelling in the northern Red Sea lead to the shoaling of the mixed
490 layer at ~26.5° N throughout almost the whole year.

491 The anticyclonic eddy induced by Tokar gap winds, and the wind induced turbulent mixing together
492 enhanced the deep convection and mixing along the southern side of the Tokar jet axis during the summer,
493 while the wind induced mixing is reduced by the cyclonic eddy. This leads to a deepening of the mixed
494 layer, to >40 m, while the MLDs in the rest of the Red Sea are <20 m. The effect of Tokar event is seen
495 in the profiles of late July to early August which gradually disappeared by October. The frequent eddies,
496 associated with surface circulation and Tokar events, have strong impact on the MLD structure of the Red
497 Sea.

Deleted: The Tokar gap winds during the summer enhanced the deep convection and mixing along the southern side of the Tokar jet axis.

Deleted: August, and

Deleted: is

509 **Data availability**

510 The climatology data produced in this manuscript is available from the repository "Figshare"
511 (DOI:10.6084/m9.figshare.5539852). The monthly mean values of heat fluxes and wind stress data are
512 available from Tropflux (http://www.incois.gov.in/tropflux_datasets/data/monthly/). The monthly mean
513 values of evaporation is available from OAflux
514 (ftp://ftp.whoi.edu/pub/science/oaflux/data_v3/monthly/evaporation/). The precipitation data is available
515 from TRMM (<https://pmm.nasa.gov/data-access/downloads/trmm>).

516 **Acknowledgments**

517 This project was funded by the Deanship of Scientific Research (DSR), King Abdulaziz University, under
518 grant number (438/150/129). The authors, therefore, acknowledge the DSR's technical and financial
519 support. The authors acknowledge TropFlux, OAFlux, TRMM, AVISO, CFSR, World Ocean Database
520 and Coriolis data center for making their data products publicly available. The authors also [acknowledge](#)
521 the institutes who have provided CTD profiles from different cruises. The author CPA acknowledges the
522 Deanship of Graduate Studies, King Abdulaziz University, Jeddah, for providing a Ph.D. Fellowship.

523 **References**

524 Abdulla, C. P., Alsaafani, M. A., Alraddadi, T. M. and Albarakati, A. M.: Estimation of Mixed Layer
525 Depth in the Gulf of Aden: A New Approach, PLoS One, 11(10), e0165136,
526 doi:10.1371/journal.pone.0165136, 2016.

527 Aboobacker, V. M., Shanas, P. R., Alsaafani, M. A. and Albarakati, A. M.: Wave energy resource
528 assessment for Red Sea, Renew. Energy, 1–13, doi:10.1016/j.renene.2016.09.073, 2016.

529 Albarakati, A. M. and Ahmad, F.: Variation of the surface buoyancy flux in the Red Sea, Indian J. Mar.
530 Sci., 42(6), 717–721, 2013.

Deleted: acknowledges

532 Alsaafani, M. A. and Sheno, S. S. C.: Seasonal cycle of hydrography in the Bab el Mandab region,
533 southern Red Sea, *J. Earth Syst. Sci.*, 113(3), 269–280, doi:10.1007/BF02716725, 2004.

534 Beal, L. M., Field, A. and Gordon, A. L.: Spreading of Red Sea overflow waters in the Indian Ocean, *J.*
535 *Geophys. Res.*, 105(C4), 8549–8564, doi:10.1029/1999JC900306, 2000.

536 Bower, A. S. and Farrar, J. T.: Air-sea interaction and horizontal circulation in the Red Sea, in *The Red*
537 *Sea*, pp. 329–342, Springer., 2015.

538 Boyer, T. P. and Levitus, S.: Quality control and processing of historical temperature, salinity, and
539 oxygen data, NOAA Tech. Rep., NESDIS 81, 65, 1994.

540 de Boyer Montegut, C., Madec, G., Fischer, A. S., Lazar, A. and Iudicone, D.: Mixed layer depth over
541 the global ocean: An examination of profile data and a profile-based climatology, *J. Geophys. Res. C*
542 *Ocean.*, 109(12), 1–20, doi:10.1029/2004JC002378, 2004.

543 Carlson, D. F., Fredj, E. and Gildor, H.: The annual cycle of vertical mixing and restratification in the
544 Northern Gulf of Eilat/Aqaba (Red Sea) based on high temporal and vertical resolution observations,
545 *Deep. Res. Part I Oceanogr. Res. Pap.*, 84, 1–17, doi:10.1016/j.dsr.2013.10.004, 2014.

546 Chelton, D. B., Schlax, M. G., Freilich, M. H. and Milliff, R. F.: Satellite measurements reveal
547 persistent small-scale features in ocean winds, *Science* (80-.), 303(5660), 978–983, 2004.

548 Chelton, D. B., Schlax, M. G. and Samelson, R. M.: Global observations of nonlinear mesoscale eddies,
549 *Prog. Oceanogr.*, 91(2), 167–216, doi:10.1016/j.pocean.2011.01.002, 2011.

550 Chen, D., Busalacchi, A. J. and Rothstein, L. M.: The roles of vertical mixing, solar radiation, and wind
551 stress in a model simulation of the sea surface temperature seasonal cycle in the tropical Pacific Ocean,
552 *J. Geophys. Res.*, 99(C10), 20345, doi:10.1029/94JC01621, 1994.

553 Cheng, L., Zhu, J., Cowley, R., Boyer, T. P. and Wijffels, S.: Time, probe type, and temperature
554 variable bias corrections to historical expendable bathythermograph observations, *J. Atmos. Ocean.
555 Technol.*, 31(8), 1793–1825, doi:10.1175/JTECH-D-13-00197.1, 2014.

556 Clifford, M., Horton, C., Schmitz, J. and Kantha, L. H.: An oceanographic nowcast/forecast system for
557 the Red Sea, *J. Geophys. Res. Ocean.*, 102(C11), 25101–25122, doi:10.1029/97JC01919, 1997.

558 D’Ortenzio, F., Iudicone, D., de Boyer Montegut, C., Testor, P., Antoine, D., Marullo, S., Santoleri, R.
559 and Madec, G.: Seasonal variability of the mixed layer depth in the Mediterranean Sea as derived from
560 in situ profiles, *Geophys. Res. Lett.*, 32(12), L12605, doi:10.1029/2005GL022463, 2005.

561 Dewar, W. K.: Mixed layers in Gulf Stream rings, *Dyn. Atmos. Ocean.*, 10(1), 1–29, 1986.

562 Ducet, N., Le Traon, P. Y. and Reverdin, G.: Global high-resolution mapping of ocean circulation from
563 TOPEX/Poseidon and ERS-1 and -2, *J. Geophys. Res. Ocean.*, 105(C8), 19477–19498,
564 doi:10.1029/2000JC900063, 2000.

565 Fox-Kemper, B., Ferrari, R. and Hallberg, R.: Parameterization of Mixed Layer Eddies. Part I: Theory
566 and Diagnosis, *J. Phys. Oceanogr.*, 38(6), 1145–1165, doi:10.1175/2007JPO3792.1, 2008.

567 Hausmann, U., McGillicuddy, D. J. and Marshall, J.: Observed mesoscale eddy signatures in Southern
568 Ocean surface mixed-layer depth, *J. Geophys. Res. Ocean.*, 122(1), 617–635,
569 doi:10.1002/2016JC012225, 2017.

570 Jiang, H., Farrar, J. T., Beardsley, R. C., Chen, R. and Chen, C.: Zonal surface wind jets across the Red
571 Sea due to mountain gap forcing along both sides of the Red Sea, *Geophys. Res. Lett.*, 36(19), 1–6,
572 doi:10.1029/2009GL040008, 2009.

573 Johns, W. E., Jacobs, G. A., Kindle, J. C., Murray, S. P. and Carron, M.: Arabian Marginal Seas and

574 Gulfs, University of Miami, Florida, USA., 1999a.

575 Johns, W. E., Jacobs, G. A., Kindle, J. C., Murray, S. P. and Carron, M.: Arabian marginal seas and
576 gulfs. University of Miami RSMAS Technical Report., University of Miami, Florida, USA., 1999b.

577 Kara, A. B., Rochford, P. A. and Hurlburt, H. E.: Mixed layer depth variability over the global ocean, *J.*
578 *Geophys. Res.*, 108(C3), 3079, doi:10.1029/2000JC000736, 2003.

579 Keerthi, M. G., Dyn, C., Monte, C. D. B., Lengaigne, M., Vialard, J., Boyer Montégut, C.,
580 Muraleedharan, P. M., Dyn, C., Monte, C. D. B., Keerthi, M. G., Lengaigne, M., Vialard, J., Boyer
581 Montégut, C., Muraleedharan, P. M., de Boyer Montégut, C. and Muraleedharan, P. M.: Interannual
582 variability of the Tropical Indian Ocean mixed layer depth, *Clim. Dyn.*, 40(3–4), 743–759,
583 doi:10.1007/s00382-012-1295-2, 2012.

584 Keerthi, M. G., Lengaigne, M., Drushka, K., Vialard, J., Montegut, C. D. B., Pous, S., Levy, M. and
585 Muraleedharan, P. M.: Intraseasonal variability of mixed layer depth in the tropical Indian Ocean, *Clim.*
586 *Dyn.*, 46(7–8), 2633–2655, doi:10.1007/s00382-015-2721-z, 2016.

587 Lorbacher, K., Dommenges, D., Niiler, P. P. and Köhl, A.: Ocean mixed layer depth: A subsurface
588 proxy of ocean-atmosphere variability, *J. Geophys. Res. Ocean.*, 111(7), 1–22,
589 doi:10.1029/2003JC002157, 2006.

590 Papadopoulos, V. P., Zhan, P., Sofianos, S. S., Raitzos, D. E., Qurban, M., Abualnaja, Y., Bower, A. S.,
591 Kontoyiannis, H., Pavlidou, A., Asharaf, T. T. M., Zarokanellos, N. and Hoteit, I.: Factors governing
592 the deep ventilation of the Red Sea, *J. Geophys. Res. Ocean.*, 120(11), 7493–7505,
593 doi:10.1002/2015JC010996, 2015.

594 Polovina, J., Mitchum, G. T. and Evans, T.: Decadal and basin-scale variation in mixed layer depth and
595 the impact on biological production in the Central and North Pacific , 1960-88, *Deep Sea Res.*, 42(10),

596 1701–1716, 1995.

597 Praveen Kumar, B., Vialard, J., Lengaigne, M., Murty, V. S. N. and McPhaden, M. J.: TropFlux: air-sea
598 fluxes for the global tropical oceans—description and evaluation, *Clim. Dyn.*, 38(7–8), 1521–1543,
599 doi:10.1007/s00382-011-1115-0, 2012.

600 Praveen Kumar, B., Vialard, J., Lengaigne, M., Murty, V. S. N., McPhaden, M. J., Cronin, M. F.,
601 Pinsard, F. and Gopala Reddy, K.: TropFlux wind stresses over the tropical oceans: evaluation and
602 comparison with other products, *Clim. Dyn.*, 40(7–8), 2049–2071, doi:10.1007/s00382-012-1455-4,
603 2013.

604 Quadfasel, D. and Baudner, H.: Gyre-scale circulation cells in the red-sea, *Oceanol. Acta*, 16(3), 221–
605 229, 1993.

606 Ralston, D. K., Jiang, H. and Farrar, J. T.: Waves in the Red Sea: Response to monsoonal and mountain
607 gap winds, *Cont. Shelf Res.*, 65, 1–13, doi:10.1016/j.csr.2013.05.017, 2013.

608 Smith, K. S. and Marshall, J.: Evidence for Enhanced Eddy Mixing at Middepth in the Southern Ocean,
609 *J. Phys. Oceanogr.*, 39(1), 50–69, doi:10.1175/2008JPO3880.1, 2009.

610 Sofianos, S. S. and Johns, W. E.: Observations of the summer Red Sea circulation, *J. Geophys. Res.*
611 *Ocean.*, 112(6), 1–20, doi:10.1029/2006JC003886, 2007.

612 Sofianos, S. S., Johns, W. E. and Murray, S. P.: Heat and freshwater budgets in the Red Sea from direct
613 observations at Bab el Mandeb, *Deep. Res. Part II Top. Stud. Oceanogr.*, 49(7–8), 1323–1340,
614 doi:10.1016/S0967-0645(01)00164-3, 2002.

615 Sutton, P. J., Worcester, P. F., Masters, G., Cornuelle, B. D. and Lynch, J. F.: Ocean mixed layers and
616 acoustic pulse propagation in the Greenland Sea, *J Acoust Soc Am*, 94(3), 1517–1526,

617 doi:10.1121/1.408130, 2014.

618 Tragou, E., Garrett, C., Outerbridge, R. and Gilman, C.: The Heat and Freshwater Budgets of the Red
619 Sea, *J. Phys. Oceanogr.*, 29(10), 2504–2522, doi:10.1175/1520-
620 0485(1999)029<2504:THAFBO>2.0.CO;2, 1999.

621 Le Traon, P. Y. and Dibarboure, G.: Mesoscale Mapping Capabilities of Multiple-Satellite Altimeter
622 Missions, *J. Atmos. Ocean. Technol.*, 16(9), 1208–1223, doi:10.1175/1520-
623 0426(1999)016<1208:MMCOMS>2.0.CO;2, 1999.

624 Turner, J. S.: *Buoyancy effects in fluids*, Cambridge University Press, Cambridge., 1973.

625 Yao, F., Hoteit, I., Pratt, L. J., Bower, A. S., Zhai, P., Köhl, A. and Gopalakrishnan, G.: Seasonal
626 overturning circulation in the Red Sea: 1. Model validation and summer circulation, *J. Geophys. Res.*
627 *Ocean.*, 119(4), 2238–2262, doi:10.1002/2013JC009004, 2014a.

628 Yao, F., Hoteit, I., Pratt, L. J., Bower, A. S., Köhl, A., Gopalakrishnan, G. and Rivas, D.: Seasonal
629 overturning circulation in the Red Sea: 2. Winter circulation, *J. Geophys. Res. Ocean.*, 119(4), 2263–
630 2289, doi:10.1002/2013JC009331, 2014b.

631 Zeng, L. and Wang, D.: Seasonal variations in the barrier layer in the South China Sea: characteristics,
632 mechanisms and impact of warming, *Clim. Dyn.*, 48(5–6), 1911–1930, doi:10.1007/s00382-016-3182-
633 8, 2017.

634 Zhai, P. and Bower, A. S.: The response of the Red Sea to a strong wind jet near the Tokar Gap in
635 summer, *J. Geophys. Res. Ocean.*, 118(1), 422–434, doi:10.1029/2012JC008444, 2013.

636 Zhan, P., Subramanian, A. C., Yao, F. and Hoteit, I.: Eddies in the Red Sea: A statistical and dynamical
637 study, *J. Geophys. Res. Ocean.*, 119(6), 3909–3925, doi:10.1002/2013JC009563, 2014.

